Implications of Both Statistical Equilibrium and Global Warming Simulations with CCSM3. Part I: On the Decadal Variability in the North Pacific Basin

MARC D'ORGEVILLE AND W. RICHARD PELTIER

Department of Physics, University of Toronto, Toronto, Ontario, Canada

(Manuscript received 15 January 2008, in final form 30 April 2009)

ABSTRACT

In the low-resolution version of the Community Climate System Model, version 3 (CCSM3), the modeled North Pacific decadal variability is demonstrated to be independent of the epoch for which a statistically steady control simulation is constructed, either preindustrial or modern; however, it is demonstrated to be significantly affected by the different global warming scenarios investigated.

In the control simulations, the North Pacific basin is shown to be dominated by sea surface temperature (SST) variability with a time scale of approximately 20 yr. This mode of variability is in close accord with the observed characteristics of the Pacific decadal oscillation (PDO). A detailed analysis of the statistical equilibrium runs is performed based on other model variables as well [sea surface salinity (SSS), barotropic circulation, freshwater and heat fluxes, wind stress curl, sea ice, and snow coverage]. These analyses confirm that the underlying mechanism of the PDO involves a basin-scale mode of ocean adjustment to changes of the atmospheric forcing associated with the Aleutian low pressure system. However, they also suggest that the observed sign reversal of the PDO arises from a feedback in the northern part of the basin. In this novel hypothesis, the advection to the Bering Sea of ''spice'' anomalies formed in the central and western Pacific sets up a typical 10-yr time scale for the triggering of the PDO reversal.

In all of the global warming simulations described in this paper, the signal represented by the detrended SST variability in the North Pacific displays significant power at multidecadal frequencies. In these simulations, the natural North Pacific decadal variability, as characterized in the control simulations (the PDO), remains the leading mode of variability only for moderate forcing. If the warming is too strong, then the typical 20-yr time scale of the canonical PDO can no longer be detected, except in terms of SSS variability and only prior to a significant change that occurs in the Bering Strait Throughflow.

1. Introduction

In the North Pacific basin, low-frequency variability in sea surface temperature (SST) has been observed to be characterized by a decadal time scale. Commonly referred to as the Pacific decadal oscillation (PDO; Mantua et al. 1997), the spatial pattern of this mode has a characteristic ''horseshoe'' shape, with opposite signs between the extremum in the western and central Pacific and that localized to the eastern rim of the basin. Its time evolution displays characteristic decadal variability (Latif and Barnett 1996) superimposed on a lower-frequency modulation (Minobe 1997; d'Orgeville and Peltier 2007), consisting of periods of stable sign separated by abrupt sign reversals as, for instance, in the case of the well-known 1976/77 climate shift (Trenberth and Hurrell 1994; Latif and Barnett 1996).

The PDO has been shown to have an impact on North American climate (Zhang et al. 1997), and to modulate the effects of El Niño–Southern Oscillation (ENSO) over North America (Gershunov and Barnett 1998; McCabe and Dettinger 1999). More generally, understanding the natural variability of the climate system is particularly important to an improved assessment of the observed ongoing global warming and to our expectation of the way in which the natural variability and forced warming may interact in the future. In the North Pacific, the spatial pattern of SST warming displays a maximum located in the center of action of the PDO (i.e., in the central and western part of the basin, as shown, e.g., in the twentieth-century simulation presented

Corresponding author address: Marc d'Orgeville, Climate Change Research Centre, Faculty of Science, UNSW, Sydney 2052, NSW, Australia.
E-mail: marcdo@unsw.edu.au

DOI: 10.1175/2009JCLI2428.1

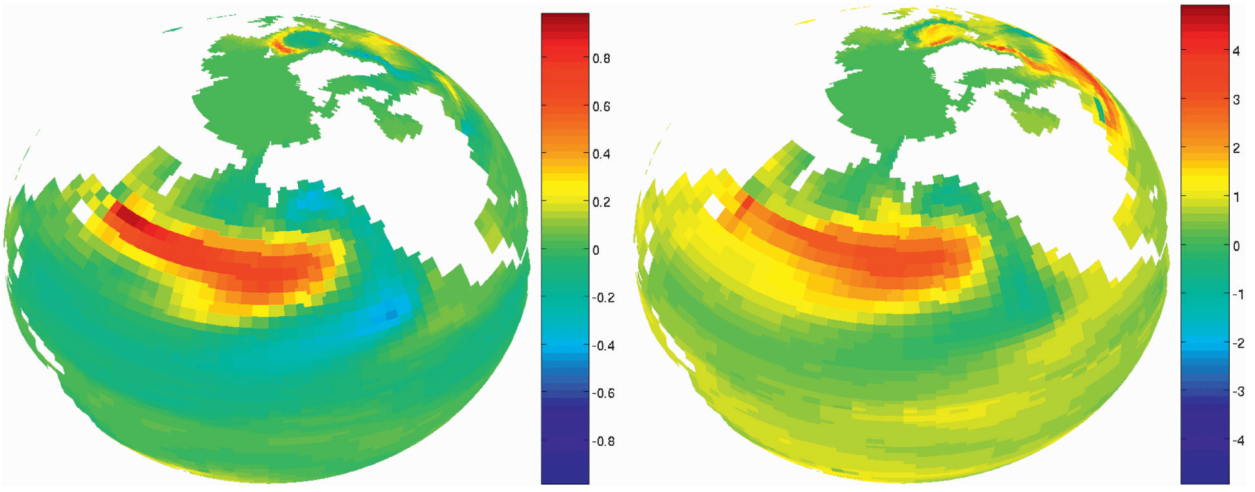

FIG. 1. Comparison for the twentieth-century simulation of (left) the PDO SST pattern (SST1 in NP) and (right) the warming SST pattern (difference between the periods 1870–79 and 1990–99). Color bars are in °C.

herein; Fig. 1). This suggests that greenhouse gas–induced warming could interact with the PDO.

Based on analysis of multicentury integrations performed using the Community Climate System Model, version 3 (CCSM3), atmosphere–ocean coupled general circulation model (AOGCM), the first goal of this paper is therefore to demonstrate that global warming may be expected to exert a strong influence on the natural North Pacific decadal variability. To establish the validity of this conjecture, however, it is necessary to first characterize North Pacific decadal variability in appropriate control simulations in relation to its current understanding in the literature.

From an observational perspective, there is strong evidence of a linkage between the PDO and processes occurring in the Indo-Pacific tropical ocean. Many authors (Trenberth and Hurrell 1994; Zhang et al. 1997; Gu and Philander 1997; Deser et al. 2004) argue that North Pacific decadal variability is in fact forced by variations in the tropical Pacific through atmospheric teleconnections. Some ''tropical theories'' argue specifically for a tropically forced mechanism where atmospheric teleconnections from the tropics are assumed to impact North Pacific SST decadal variability, either by a direct transfer of the tropical decadal variability (Trenberth 1990), or by ENSO-related interannual forcing, which is subsequently integrated or ''reddened'' by the winter SST reemergence mechanism (Newman et al. 2003). Still, other tropical theories advocate a tropical–extratropical coupling mechanism in which atmospheric teleconnections involve a tropics to subtropics pathway (Alexander et al. 2002; Vimont et al. 2001), whereas the decadal time scale is set by the ocean because of its adjustment to thermal anomalies from the midlatitudes to the tropics, either by adiabatic advection (Gu and Philander 1997) or diabatic processes (Boccaletti et al. 2005).

Although the understanding of tropical–extratropical teleconnections on decadal time scales is of primary importance in the study of the decadal modulation of the El Niño–Southern Oscillation phenomenon, these teleconnections do not seem to constitute sufficient conditions for the existence of the PDO. Indeed, AOGCM simulations deliver a reasonable depiction of the PDO, even in the absence of any strong connection to the tropical Pacific (i.e., Alexander et al. 2006; Latif 2006; Kwon and Deser 2007). Recently, Zhong et al. (2007) have argued convincingly that the Pacific multidecadal variability in CCSM3 finds its origin exclusively in the midlatitudes.

These ''midlatitude theories'' originated in the seminal studies of Latif and Barnett (1994, 1996), who suggested, mainly based on the results of numerical simulations, that the decadal variability in the North Pacific could be attributed to a cycle involving ocean–atmosphere interaction between the subtropical ocean gyre circulation and the atmospheric Aleutian low pressure system. Since then, the main question that has been debated concerning these numerical simulation–based hypotheses (Pierce et al. 2001; Schneider et al. 2002) concerns the issue as to whether the decadal spectral peak is maintained by a coupled ocean–atmosphere mode of internal variability (Neelin and Weng 1999) or arises from a damped ocean-only mode that is continuously excited by atmospheric stochastic forcing (Saravanan and McWilliams 1998).

In both scenarios, the time scale of the observed variability is thought to derive from the propagation of baroclinic Rossby waves across the basin that are triggered by the geostrophic adjustment to the surface

TABLE 1. List of simulations with run characteristics.

Run name	Forcing	Duration	Analysis on	Initial yr	From run
1870-control	1870 annual cycle	1100	2270–2569	1870	Start-up
1870–0.5%	Increase of 0.5% CO_2 yr^{-1}	200	2370–2569	2370	1870-control
1870–1.0%	Increase of 1.0% CO_2 yr^{-1}	200	2370–2569	2370	1870-control
1870–2000	Twentieth century	130	1870–1999	2370	1870-control
1990-control	1990 annual cycle	705	400–700	1	Start-up
1990–0.5%	Increase of 0.5% CO_2 yr^{-1}	200	506–705	506	1990-control
1990–1.0%	Increase of 1.0% CO_2 yr^{-1}	200	506–705	506	1990-control

forcing and influenced by mean oceanic currents. However, although such geostrophic adjustment has been invoked, numerical studies on the PDO have focused exclusively on the temperature variability, probably because of the way in which the PDO is characterized in the observations. The observed decadal salinity variability along the coast of North America, on the other hand, has not been directly related to the PDO but rather to a distinct Pacific mode of variability (Di Lorenzo et al. 2008). The second goal of this paper will be to demonstrate that salinity plays an active role in the development of the PDO in the simulations presented herein; an explanation of the PDO time scale delivered by the model will be provided based on this extension to the usual analysis.

This article is organized as follows: in section 2, the numerical simulations to be analyzed in this paper are described, as well as the spatial and temporal filtering of the outputs to be employed and the technical aspects of the analyses to be performed. Sections 3–6 present the decadal variability in the control simulations. Section 3 characterizes the modeled PDO in terms of both SST and sea surface salinity (SSS), and it provides a comparison to observations. The variability of surface fluxes is related to the ocean variability in section 4. Section 5 displays a typical evolution of the PDO from the surface, and section 6 discusses the origins of the PDO time scale in our simulations. Finally, the effect of global warming on North Pacific decadal variability is examined in section 7. Section 8 summarizes our findings and provides a discussion of their implications.

2. Numerical experiments and analysis procedures

a. The coupled atmosphere–ocean climate model

The model employed in this study is the CCSM3. The model has four interacting components—atmosphere, ocean, sea ice, and land surface—linked via a flux coupler. All of the simulations discussed in the following have been performed at T31 resolution for the atmospheric component (26 vertical levels and 3.75° horizontal resolution) and with a grid termed gx3v5 for the oceanic component (25 vertical levels, 3.6° resolution in the zonal direction, and variable in the meridional direction with approximately 0.6° resolution near the equator). A detailed description of the model can be found in Collins et al. (2006), and a detailed description of this specific resolution can be found in Yeager et al. (2006).

The simulations consist primarily of two ''control'' computations under perpetual annual cycle forcing corresponding to 1870 and 1990 epoch climate conditions, with durations of 1100 and 700 yr, respectively. The period of 400–700 yr of these 1870 and 1990 runs, to be referred to as 1870-control and 1990-control, respectively, are employed as the basis for the analyses reported in sections 3–6.[1]

The two spinup runs have been further employed to provide two sets of initial conditions (at 500 yr) for a series of global warming simulations. From each spinup run, two 200-yr simulations forced by a constant rate of increase of 0.5% and 1% in CO_2 concentration per year have been branched off, with all other parameters kept fixed to those employed in the corresponding control run. A complete simulation of twentieth-century warming has also been performed from 1870 to 2000 as a continuation of the 1870 statistical equilibrium run with all climatic parameters evolving based on reconstructions described in Meehl et al. (2006): greenhouse gas concentrations, solar and volcanic forcing, sulfate aerosols, and ozone. The results obtained from these five warming simulations are described in section 7. The reference names and properties of each of the seven simulations are summarized in Table 1.

b. Filtering procedures and diagnostic analyses

Because this study focuses on decadal to multidecadal time-scale variability, all the diagnostics presented will be based on low-pass filtered annual anomalies. These anomalies have been created by using a three-step diagnostic procedure: first, annual averages are computed from the monthly output; next, the mean and linear trends are removed to produce anomaly fields; and

[1] Note that the same results are found if the period 400–1100 yr of the 1870 run is used instead of the period 400–700 yr.

finally, a low-pass filter based on a 10-yr width Hanning window is applied to all time series.

Classical empirical orthogonal function (EOF) analyses, with area-weighted time series, have been conducted on different variables for the North Pacific region defined as extending from 20° to 65°N and from 120°E to 100°W (hereafter, NP region). In the following, principal components (PCs) correspond to the time series of the evolution of the amplitude of each of the different EOFs, whereas the spatial pattern of the EOF is plotted over the entire North Pacific basin after a regression at every grid point on its corresponding PC. The PCs are normalized by their standard deviation and are therefore unit variance time series. Consequently, the EOF spatial patterns have the dimension of the corresponding analyzed variable and their amplitude is relative to one standard deviation of their corresponding PCs.

Statistical significance of all the regression/correlation coefficients is assessed with a two-tailed Student's *t* test, taking into account effective degrees of freedom following Bretherton et al. (1999).

Power spectrum analyses based on a single periodogram are employed on ''associated time series'' obtained by projecting raw (unfiltered) data onto the EOF spatial patterns to ensure that time filters do not create artificial peaks (Saravanan and McWilliams 1997). The confidence levels, shown in all related plots, are based on reference red-noise spectra with the same total variance and the same lag-1 autocorrelations as the analyzed time series (Mann and Lees 1996).

Fluxes are computed across the ocean surface from the atmosphere or the ice components to the ocean component, with a positive flux representing a gain by the ocean. Heat flux (HFLX) is the sum of all fluxes to the ocean (shortwave, longwave, latent, sensible, and sea ice melting/formation). Freshwater flux (FWFX) is also taken to be the sum of all fluxes to the ocean (evaporation, precipitation, runoff, and sea ice melting/formation). Note that stress from the sea ice is included in the wind stress curl (WSC).

3. SST and SSS variability

The results for the decadal variability in the North Pacific presented in sections 3–6 of this paper are described only for the 1870-control simulation, because essentially identical results have been found in 1990-control. Some differences between the two simulations will be highlighted throughout the text.

The first EOF of SST in the NP region displays the classic horseshoe pattern of the observed PDO, with an amplitude maximum in the western and central part of the basin and an extremum of opposite sign along the eastern rim of the basin (Fig. 2). As in the case of the observations, the corresponding first principal component shows a clear decadal time scale of variability.

Two fundamental differences between the modeled and the observed PDO do exist. First, the amplitude of the maximum is twice that characteristic of the observations; to see this, compare Fig. 2a directly with Fig. 1a of d'Orgeville and Peltier (2007), for which the same analysis procedure has been applied to the observed SST field. Second, no second extremum is present in the tropical Pacific in the model simulations; this is clearly related to the fact that the El Niño–Southern Oscillation spectrum in CCSM3 displays a sharp peak at a 2–3-yr period with no significant power at lower frequency (Yeager et al. 2006), a bias that was already shown to be characteristic of previous versions of the National Center for Atmospheric Research (NCAR) coupled model [e.g., see the analyses reported by Peltier and Solheim (2004) that are based on the use of Climate System Model, version 1.4 (CSM1.4)]. This known bias of CCSM3 demonstrates that the modeled decadal variability might be in a different regime than the observed PDO [maybe due to the use of an unrealistic tropical convection parameterization, as discussed in Wu et al. (2007)]. The explanation of our modeled PDO must therefore be sought in (perhaps some variations of) the midlatitude theories reviewed in the introduction.

The EOFs of SSS in the NP region have also been analyzed. The first EOF of SSS displays a similar dipole pattern to the first EOF of SST, with a maximum in the west and central areas and an extremum of opposite sign in the east (Fig. 3). However, the SSS pattern is much narrower and more localized than the SST pattern (Fig. 2). These similarities and differences are directly related to the mean background of SSS and SST. Extrema are located in the vicinity of the maximum of the horizontal gradient of the mean, and this region is located, for both SST and SSS, in the vicinity of 40°N, between the subtropical and the subpolar gyres. However, because SSS has a much sharper meridional gradient than SST, SSS extrema are more localized than SST extrema. Therefore, even if the two patterns differ somewhat from each other, they are clearly associated with the same phenomenon. This is even more evident by inspection of their corresponding PCs (Figs. 2, 3), which have a correlation coefficient of 0.9, which is statistically significant at the 99% level.

Although the first EOFs have the same dipolar spatial structure, the second EOFs in SST and SSS are quite different, with a wide monopole centered in the north for SST and a localized maximum in the southeast for SSS (Figs. 2, 3). Those EOFs apparently represent different phenomena. This is confirmed by their corresponding

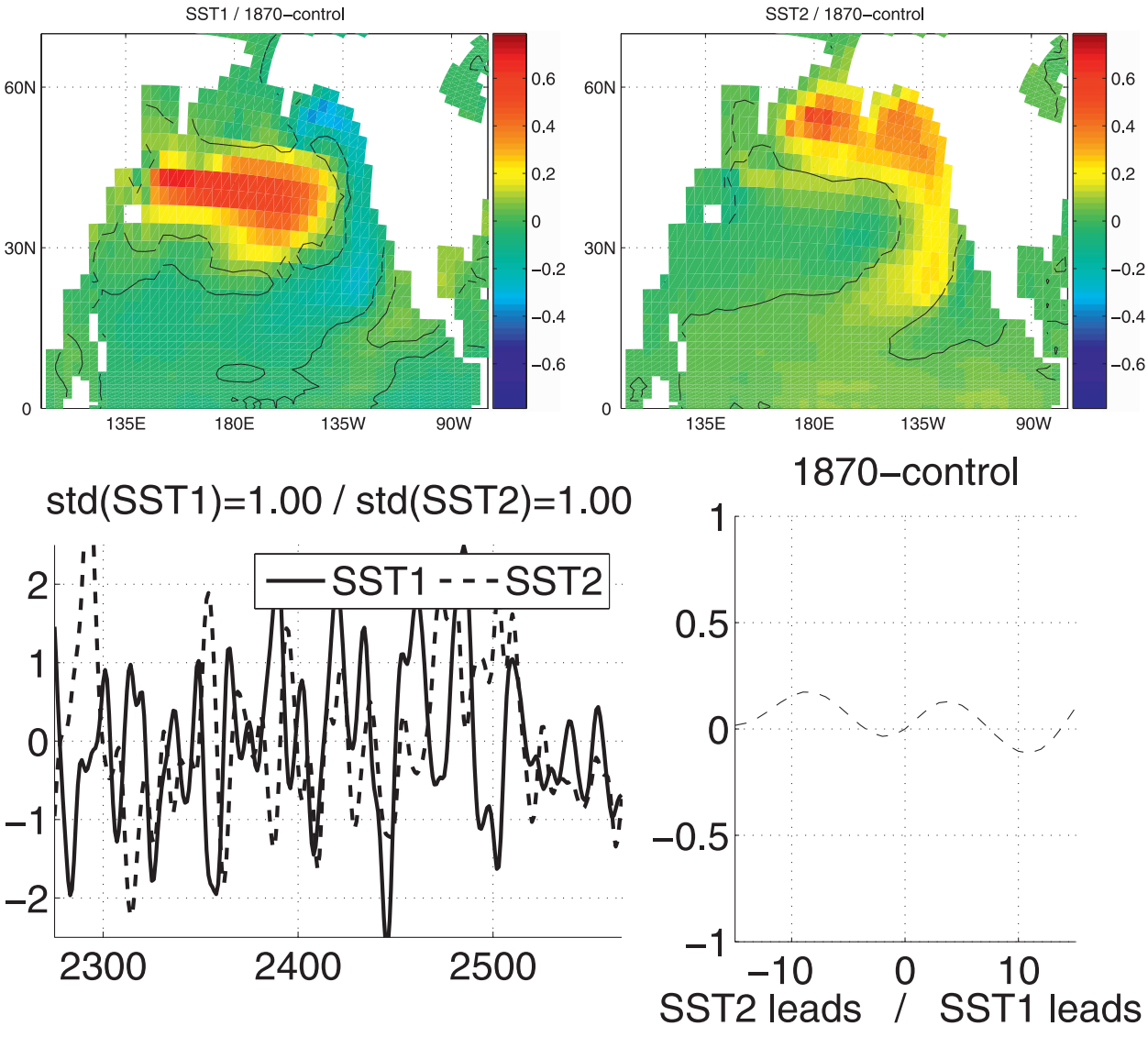

FIG. 2. EOF analysis of SST fields in the NP region of simulation 1870-control. (top left) First and (top right) second EOFs. The black dashed lines correspond to the limit of the region significant at the 90% confidence level. Color bars in °C. (bottom left) First and second PC (solid and dashed lines, respectively) and (bottom right) their time-lag correlation as a function of the lag in years. Statistical significance at the 90% (solid line), 95% (thick solid line), and 99% (large dots) levels: first and second PC are not significantly time-lag correlated here.

PCs, which have no statistically significant correlation. Moreover, whereas the first two PCs of SST do not show any time-lag correlation (Fig. 2), the first two PCs of SSS present strong time-lag correlations at lags around +5 and −5 yr (Fig. 3). This type of time-lag correlation with two extrema of opposite sign existing at two lags of opposite sign can be interpreted as representing two components in phase quadrature of the same oscillation cycle; this will be further discussed later in this paper.

To define the time scale of the PDO in our simulation, we take advantage of the existence of the millennium-long simulation at 1870 fixed climate conditions (from which the years 400–700 correspond to 1870-control), and we perform the same EOF analyses already described on the last 700 yr (from 400 to 1100). The power spectrum analyses of the associated time series of the first SST and SSS EOFs on this 700-yr control simulation reveal a dominant peak at a period of approximately 17 yr (Fig. 4). This peak is at the same frequency in both SST and SSS analyses but has a statistical significance of 95% in SST and 99% in SSS. This difference is due to less noise at interannual frequencies in SSS variability than in SST variability.

In previous CCSM control simulations at the same resolution, the PDO has been shown to have equivalent decadal peaks of an approximately 15-yr period in

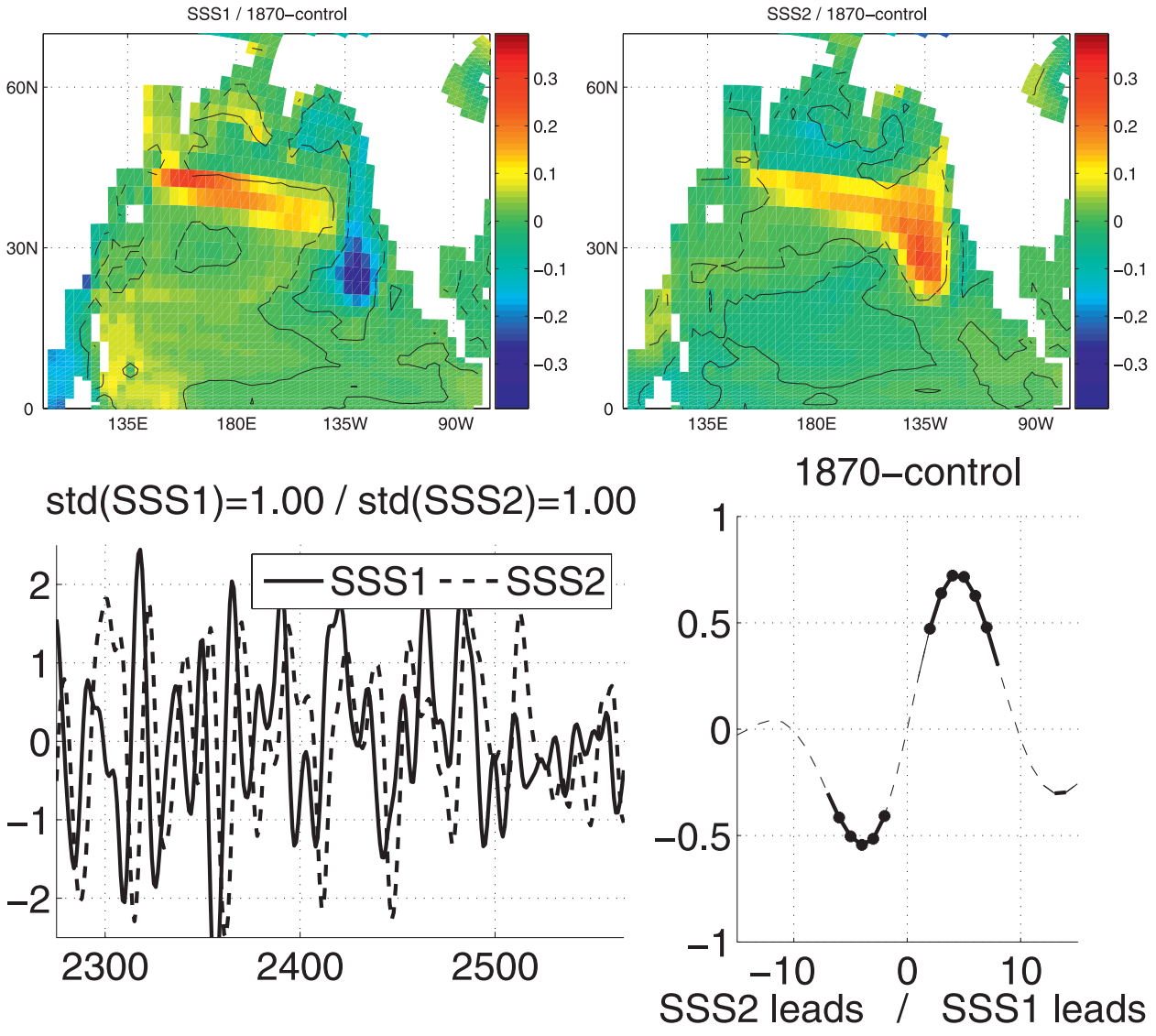

FIG. 3. As in Fig. 2, but for SSS. Color bar in psu.

CCSM2 (Kwon and Deser 2007) and of an approximately 18-yr period in CCSM3 (Zhong et al. 2007).[2] However, when computing the power spectra on only 300 yr of our millennium-long simulation, the periods of the dominant peaks are found to vary from 15 to 25 yr, depending on which 300-yr period is chosen (not shown). Although the frequency of the dominant peaks varies between different 300-yr periods, they always have the same frequency in both SST and SSS in a given 300-yr period (always with a statistical significance of 99% in SSS). Power spectra in 1870-control and 1990-control display a PDO period of 25 and 18 yr, respectively (not shown). In the following, the natural time scale of the PDO in our control simulations will therefore be referred to as being 20 yr with a period range of 15–25 yr (highlighted in gray in Fig. 4).

4. Variability in surface fluxes

To assess the relationships between the surface fluxes (heat, freshwater, and momentum) and the oceanic states involved in PDO development, this section presents EOF analysis of these surface-related variables. Specifically, the relation of the oceanic state variables with their corresponding fluxes are discussed—SST with

[2] These previous estimates are based on equivalent EOF analyses and/or from a time series index based on the average SST over the Kuroshio Extension. Our estimate does not change if the latter method is used.

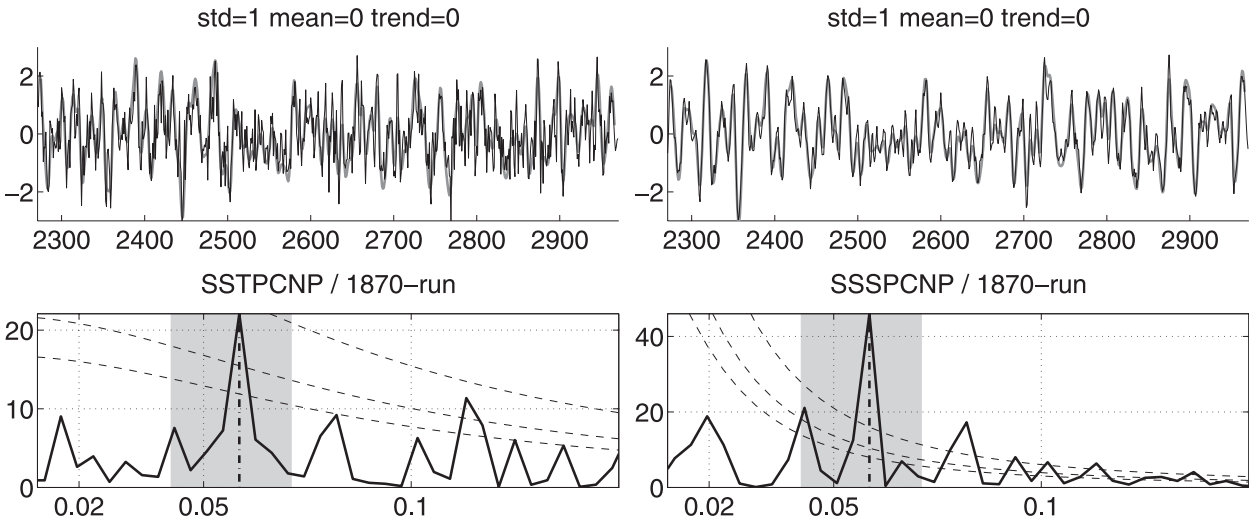

FIG. 4. (left) SST and (right) SSS time series analyses. (top) Associated time series of the first EOF (thin black line) and first PC (thick gray line). Time series have been rescaled by their standard deviation. (bottom) Power spectra of the first EOF. Dashed lines correspond to the 90%, 95%, and 99% significant levels. The gray area corresponds to the PDO frequency range (see text for details).

HFLX, SSS with FWFX, and barotropic stream function (BSF) with WSC—and a global interpretation is presented at the end of this section. The first and second EOFs of SST are denoted as SST1 and SST2, and the first and second EOFs of the other variables are denoted equivalently. The corresponding explained variances for each variable are summarized in Table 2.

The first and second EOFs for heat flux (Fig. 5) have two distinct and well-defined centers of action (global maximum of absolute anomaly): in the Bering Sea for the first and in the Kuroshio Extension region for the second. The corresponding PCs of HFLX2 and SST1 have a temporal correlation coefficient maximum for 0-yr lag. This corresponds to a loss of heat by the ocean in the Kuroshio region when this region has a positive SST anomaly (also visible in HFLX1). For the PDO, this is the well-established result that the surface heat flux acts to damp the maximum of SST anomalies of the PDO (Seager et al. 2001; Pierce et al. 2001; Schneider et al. 2002). In contrast, the corresponding PCs of HFLX1 and SST1 have their maximum of correlation coefficient when SST1 leads by 3–4 yr, which corresponds to a gain of heat by the ocean in the Bering Sea. Multiple extrema in the time-lag correlation between HFLX1 and SST1 are statistically significant at the 99% level and reflect the 20-yr time scale of the PDO. The extremum of negative correlation between HFLX1 and SST1 when HFLX1 leads by 7–8 yr shows that waters in the Bering Sea are losing heat before a positive phase of the PDO; the water advected by the western boundary current of the subpolar gyre from the Bering Sea to the Kuroshio region loses heat and is therefore unlikely to be able to explain the positive SST anomaly of the PDO. The reason for the phase lag between the Bering Sea heat flux and the PDO will be further explored in the next section.

The spatial patterns of FWFX1 and SSS1 display a spatial correspondence (Fig. 6) with negative (positive) freshwater flux anomalies located in positive (negative) SSS anomaly regions (except in the regions of the Bering and Okhotsk Seas). Because their corresponding PCs have a positive correlation coefficient for 0-yr lag, this implies that the surface fluxes play an important role in creating and/or reinforcing the SSS anomalies. In contrast, FWFX2 has its center of action located in the Bering Sea and its corresponding PC has a maximum of correlation coefficient with SSS1 when FWFX2 leads SSS1 by 4–5 yr. For FWFX2, both the delay of 4–5 yr and the location of its center of action in the Bering Sea are reminiscent of HFLX1. The particular dipole structure of FWFX2 in the Bering Sea corresponds to the retreat and/or advance of the sea ice front, which modulates the freshwater flux resulting from sea ice melting/formation closer to or farther from the coast. At lag −7 yr, the

TABLE 2. Explained variance (%) by the first two EOFs of different variables in the NP region for both control simulations.

Variable	1870-control	1990-control
SST	47–16	48–20
SSS	27–20	29–18
BSF	38–33	53–21
HFLX	22–18	23–20
FWFX	21–10	24–14
WSC	24–17	24–15

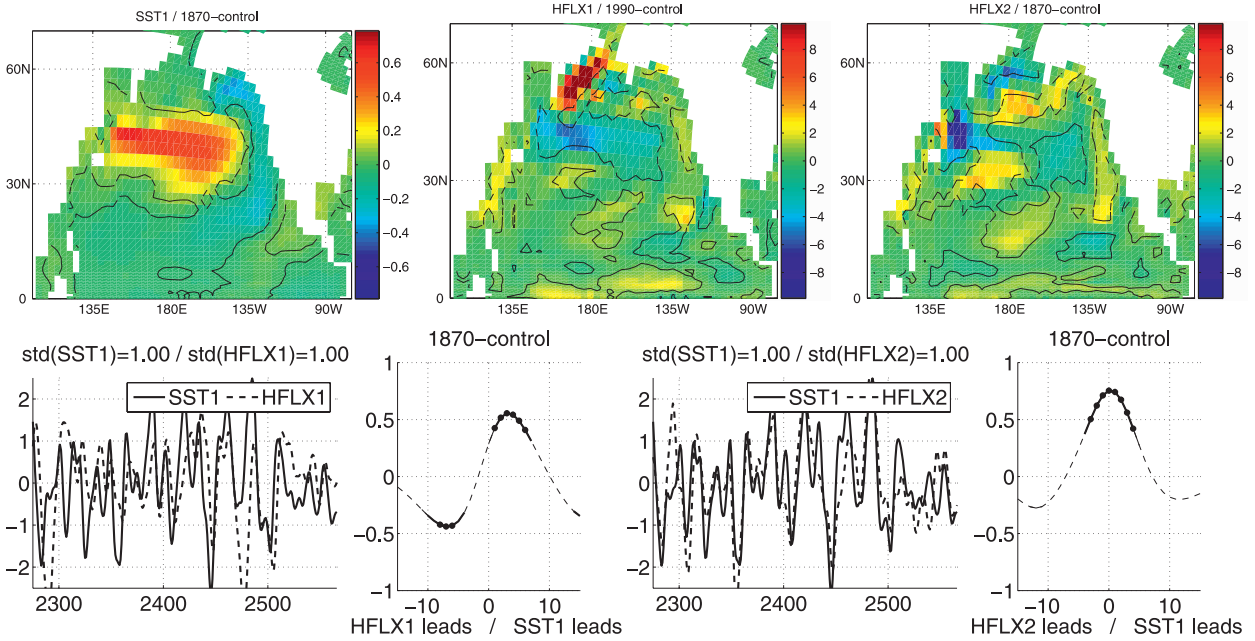

FIG. 5. (top left) SST1 (PDO pattern; reproduced from Fig. 2), (top middle) HFLX1, and (top right) HFLX2 (color bar in W m^{-2}). (bottom) SST1 (PDO index) and (bottom left) HFLX1 and (bottom right) HFLX2, with their time-lag correlation function of the lag in years (statistical significance at the 90% level indicated by solid line, 95% by thick solid line, and 99% by large dots).

negative heat anomaly of HFLX1 corresponds to more loss of heat in the Bering Sea related to a decrease of the sea ice coverage and therefore to a displacement of the freshwater flux resulting from sea ice near the coast [i.e., the negative (positive) freshwater flux anomaly far from (close to) the coast of FWFX2]. The link of causality between heat and freshwater fluxes in the Bering Sea region will be further explored in the next section.

However, note that the variability of the heat and freshwater fluxes are both dominated by the variability of evaporation and sea ice melting/formation (not shown). These phenomena affect both SST and SSS but in an

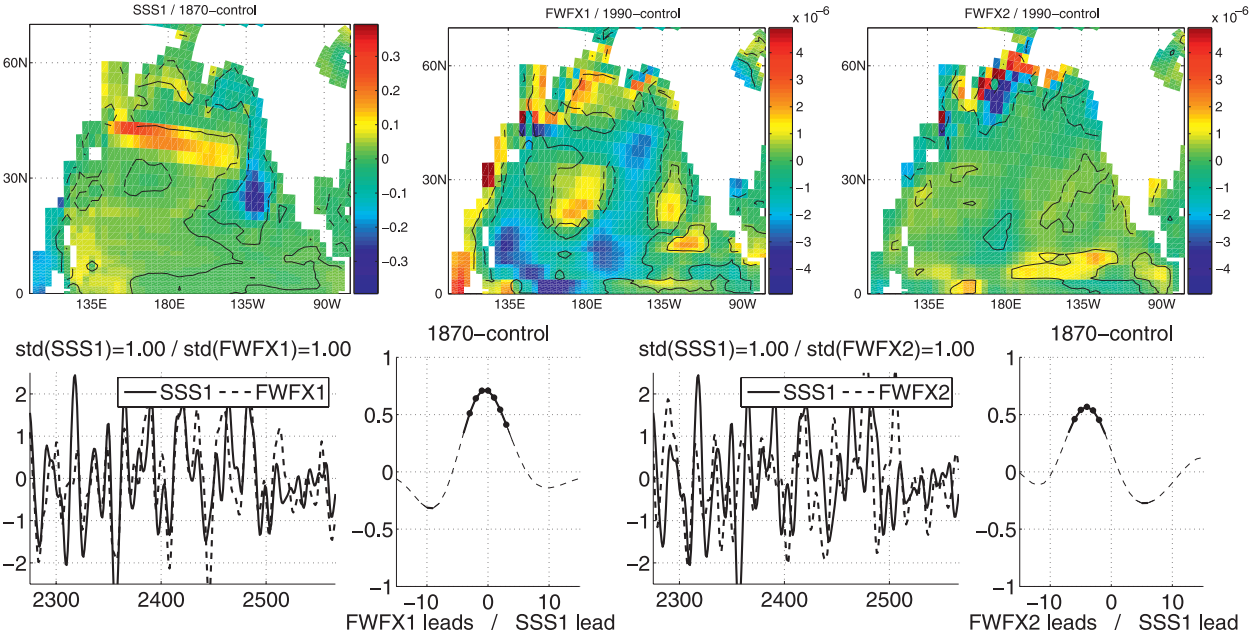

FIG. 6. As in Fig. 5, but for SSS1 (reproduced from Fig. 3), FWFX1, and FWFX2 (color bar in kg m^{-2} s^{-1}).

opposite manner; more (less) evaporation damps positive (negative) SST anomalies and reinforces positive (negative) SSS anomalies, whereas more sea ice melting (formation) damps positive (negative) SST anomalies but also damps positive (negative) SSS anomalies. Moreover, both more (less) evaporation and sea ice melting (formation) are favored by positive (negative) SST anomalies.

By comparing BSF1 and WSC1, it is apparent that BSF1 is the direct Sverdrup response to WSC1 (Fig. 7). The pattern of WSC1 corresponds to a weakening of the Aleutian low pressure system south of Alaska. The pattern of BSF1 corresponds to a shift to the north of the boundary between the subtropical and the subpolar gyres. Their corresponding PCs have their maximum of correlation coefficient at 0-yr lag, highlighting the fast barotropic adjustment to a change of the wind stress curl forcing as required by the Sverdrup balance.

Compared to the PDO index, WSC1 and BSF1 have a positive correlation at lag 0, which is in agreement with the fact that a northward shift of the boundary separating the gyres brings warm water from the subtropics and can create a positive SST anomaly in the center of action of the PDO. Note that the same mechanism can also create a positive SSS anomaly by bringing salty water from the subtropics. However the maximum of time-lag correlation between SST1 and WSC1 (or equivalently BSF1) occurs when WSC1 leads SST1 by 1 yr. This 1-yr lag suggests that other mechanisms are required to explain the creation of the SST and SSS anomalies in the center of action of the PDO. This will be further discussed in the next sections.

Finally, in terms of the surface density anomaly, the first two EOFs (which explain 22% and 20% of the variance, respectively; Fig. 8) correspond closely to the SSS EOFs, and their corresponding PCs appear to be in quadrature of phase with the SSS PCs. This demonstrates that, on decadal time scales, the variability of surface density in the North Pacific is mainly salt driven (rather than temperature driven, as it is on seasonal time scales).

The bottom line of this EOF analysis of the North Pacific from CCSM3 is that salinity is tightly coupled to the temperature in the PDO and can apparently play an important role in the decadal variability characteristic of the North Pacific Ocean. A more complete description of the mechanism involved is provided in the following sections.

5. Timing of the PDO

We describe the time-lag regressions on the PDO index of SST, SSS, BSF, wind stress curl, sea ice extent, snow coverage, and heat and freshwater fluxes, which are presented in Fig. 9. The time is therefore referenced to a lag of 0 yr, which corresponds to the maximum of SST variability but is somewhat arbitrary, because we are describing a cycle in which the maximum of other components of the variability might occur at different lags. The purpose of this section is to give an overview of a half cycle of PDO development to establish a time frame for the relations described in the previous section and to justify the rationale for the mechanism proposed for the predicted time scale of the PDO to be discussed in the following section.

At lag -6 yr, with respect to the PDO index, a dipole wind stress curl anomaly is present in the North Pacific, with a positive value in the Bering Sea and a negative value south of the Bering Sea (Fig. 9a). The small negative wind stress curl anomaly has a direct effect on the barotropic circulation, which is characterized by a small positive anomaly from the coast of Japan to the middle of the basin (Fig. 9b). From lag -6 to -2 yr, the combination of a negative wind stress curl anomaly and a positive barotropic circulation anomaly grow together to reach a maximum amplitude. At lag -2 yr, the strong negative wind stress curl anomaly is displaced to the east of the basin and corresponds to a weakening of the Aleutian low south of Alaska. By the Sverdrup relation, this induces a strong positive barotropic circulation anomaly from the coast of Japan almost to the other side of the basin, which corresponds mainly to a displacement of the boundary separating the gyres.

From lag -4 to -2 yr, the anomalous barotropic circulation brings warmer water northward, starting in the western part of the basin (Fig. 9c). This positive SST anomaly grows larger and spreads eastward until the mature phase of the SST signal is attained at lag 0 yr. Note that the maximum of the SST anomaly is achieved at lag 0 yr, whereas the barotropic circulation anomaly (and the corresponding wind stress curl anomaly) has already started to decrease between lags -2 and 0 yr. Because the surface heat flux anomaly acts to damp the SST anomaly in the west (Fig. 9d), it cannot be responsible for the final increase of the positive SST anomaly at lag 0 in the west. Continuous northward advection along the coast of Japan may explain this, as well as the baroclinic adjustment to the wind stress curl anomaly, which is delayed compared to the immediate barotropic adjustment (e.g., Kwon and Deser 2007).

However we wish to emphasize that the primary mechanism for the growth of the PDO SST anomaly appears to be the displacement of the boundary separating the gyres resulting from ''Sverdrupian'' barotropic adjustment (see also Schneider et al. 2002).

It is also believed that the growth phase of the PDO is due to a positive feedback existing between the SST and

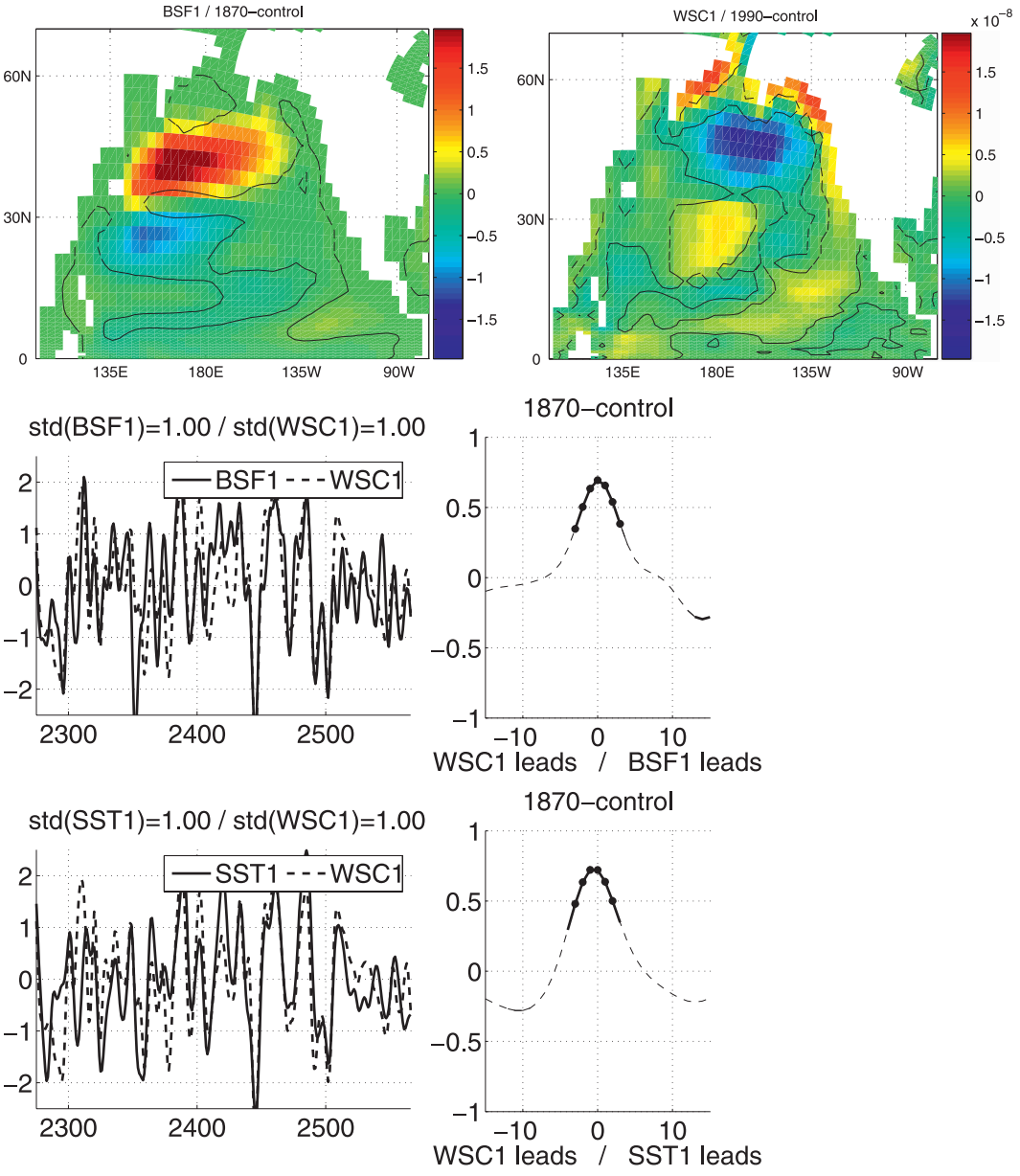

FIG. 7. (top left) BSF1 [color bar in Sv (1 Sv $\equiv 10^6$ m^3 s^{-1})] and (top right) WSC1 (color bar in N m^{-3}). Time-lag correlation curves between (middle) BSF1 and WSC1 [and (bottom) between SST1 and WSC1] as a function of the lag in years.

the Aleutian low anomaly, in which the Aleutian low anomaly creates the SST anomaly in the western part of the basin, which further reinforces the Aleutian low anomaly. This feedback must take place through the heat flux anomaly. In the Kuroshio region, the heat flux anomaly grows stronger together with the SST anomaly, which could explain the growth of the Aleutian low up to lag −2 yr. However, other regions might also play a role in setting up the wind response. For instance, the fact that the Aleutian low anomaly began to decrease after lag −2 yr might be related to the disappearance of the negative heat flux anomaly in the Bering Sea at lag 0 or to the eastward spreading of the negative heat flux from the Kuroshio region at lags 0 and 2 yr.

Eastward advection, baroclinic adjustment, and surface heat flux can all be invoked to explain the eastward spreading and the meridional broadening of the positive SST anomaly in the central part of the basin (see, e.g., Kwon and Deser 2007). In the east of the basin, the negative SST anomaly along the rim of the basin has no

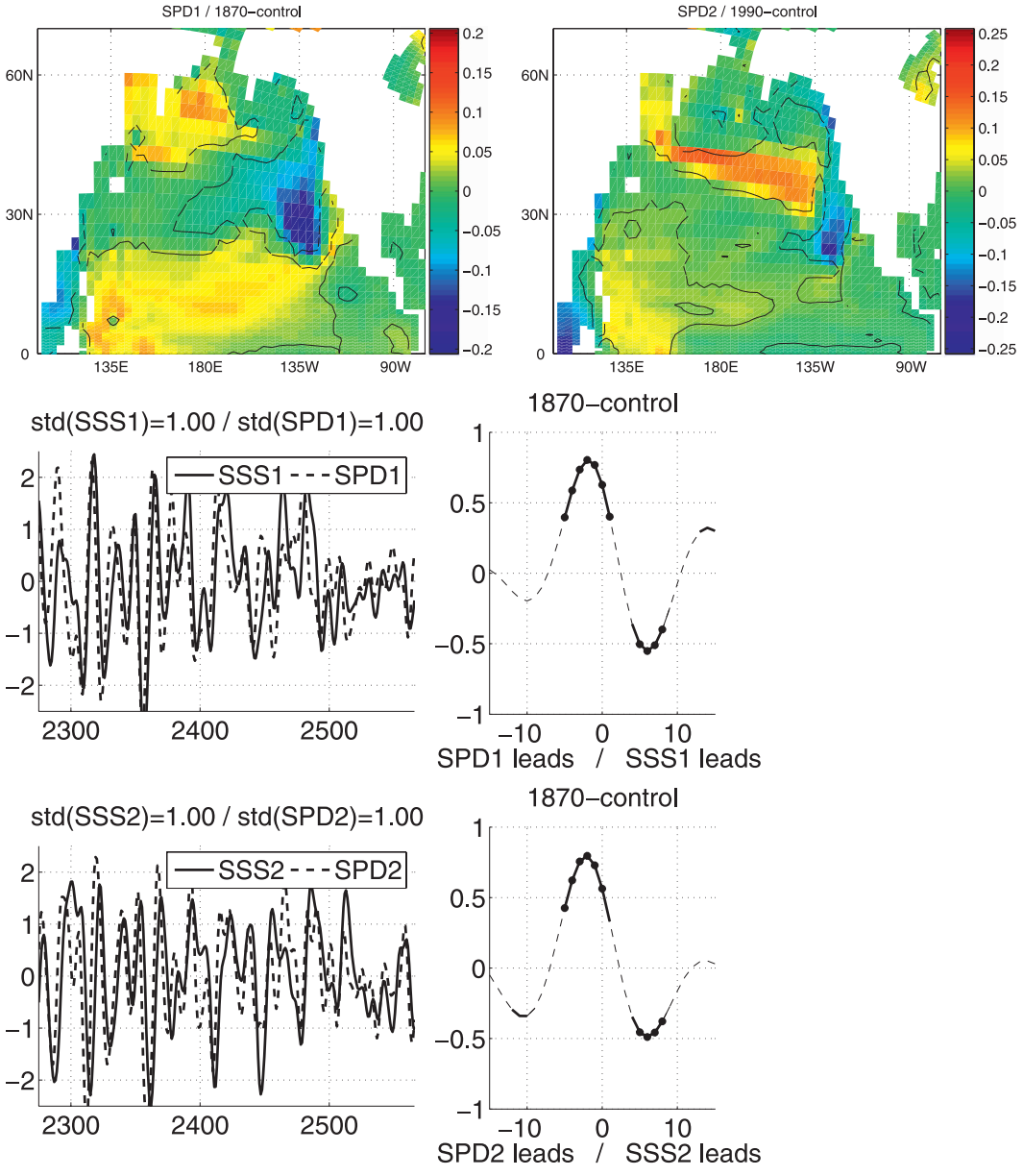

FIG. 8. (top left) First and (top right) second EOFs of the surface potential density (SPD; color bar in kg m^{-3}). Time-lag correlation curves between (middle) SPD1 and SSS1 and between (bottom) SPD2 and SSS2 as a function of the lag in years.

obvious explanation except perhaps as the consequence of the advection of the west and central negative anomaly of the previous half cycle; this advection is more clearly visible at the end of this half cycle and is described in terms of the SSS anomaly in the next paragraph. The existence of an advection mechanism will be further reinforced in the next section.

From lag −4 to 0 yr, a positive SSS anomaly develops from the west following basically the same mechanism as for the positive SST anomaly (Fig. 9e). However, as noted previously in the discussion of the EOF analysis, in contrast to the surface heat flux and SST anomalies, the surface freshwater flux anomalies reinforce the SSS anomalies (Fig. 9f). Because of the correspondence of the SSS anomalies with SST anomalies of the same sign, paired SSS–SST anomalies happen to be located where evaporation damps the SST anomaly and enhances the SSS anomaly. This is even more evident following the mature phase of the SST signal; between lag 0 and 4 yr, evaporation anomalies dominate both heat and freshwater

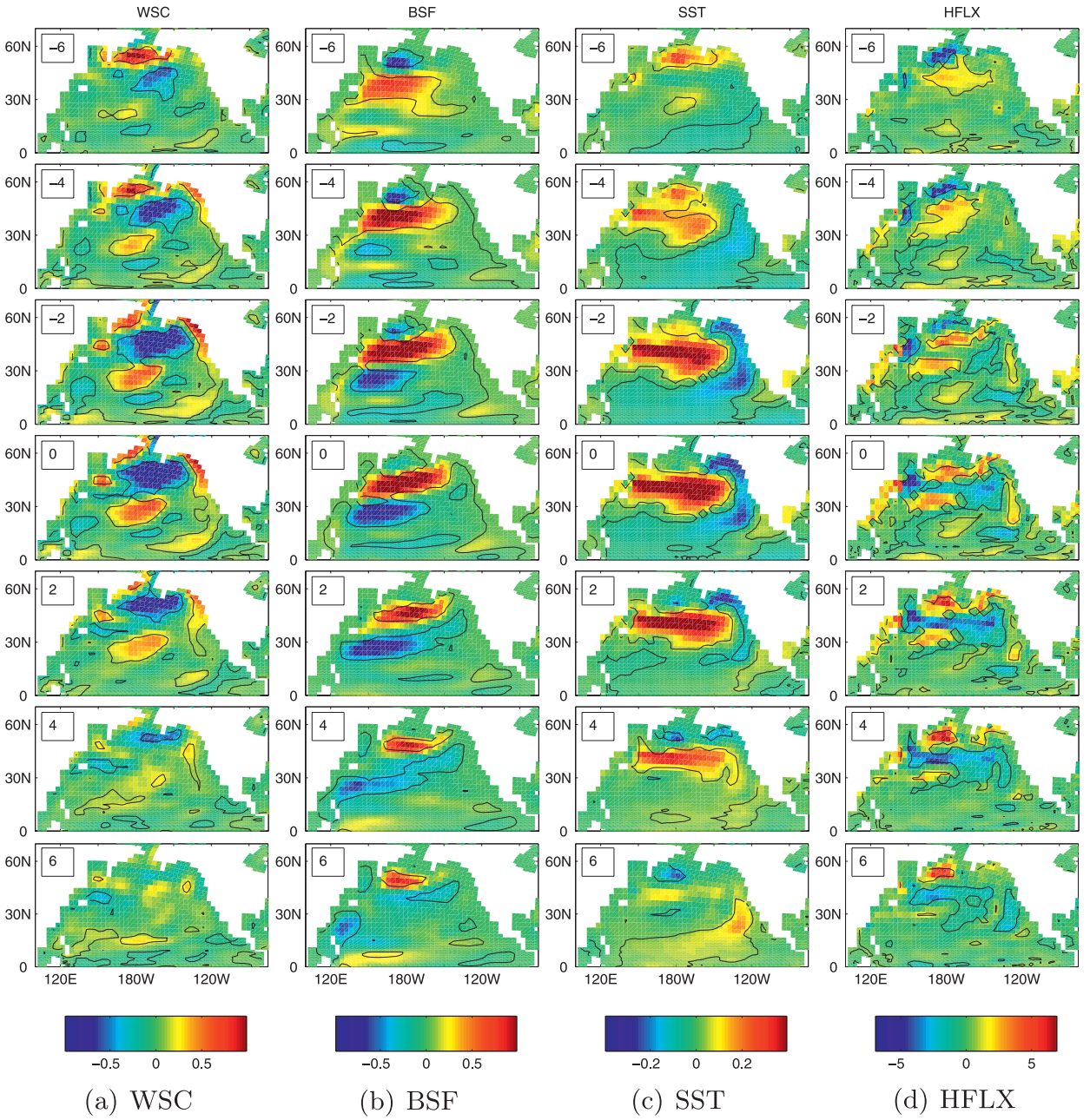

FIG. 9. Time-lag regression on the PDO index of (a) WSC (10^{-8} N m^{-3}), (b) BSF (Sv), (c) SST (°C), (d) HFLX (W m^{-2}), (e) SSS (psu), (f) FWFX (10^{-6} kg m^{-2} s^{-1}), (g) sea ice coverage (%), and (h) snow coverage (%). The corresponding lag in years is written in the top-left corner of each graphic. Black lines correspond to the limit of the 90% level of statistical significance.

fluxes, forcing SST anomalies to decline, whereas SSS anomalies are enhanced. From lag 2 to 6 yr, it is also evident that the positive SSS anomaly, which arises first in the western part of the basin, moves eastward. At lag 6 yr, it has replaced the initial negative SSS anomaly at lag −6 yr in the eastern part of the basin. From lag −6 to 6 yr, a half cycle of the oscillation has therefore been completed.

At the end of this half cycle, the Aleutian low anomaly, responsible initially for the growth of this phase of the PDO, has died out. To understand the pseudoperiodicity of the PDO, it is therefore essential to understand how a reversal of the Aleutian low anomaly can be initiated at lag 6 yr in order to start the reverse half cycle of the PDO. Because on interannual time scales the atmosphere would be expected to respond synchronously

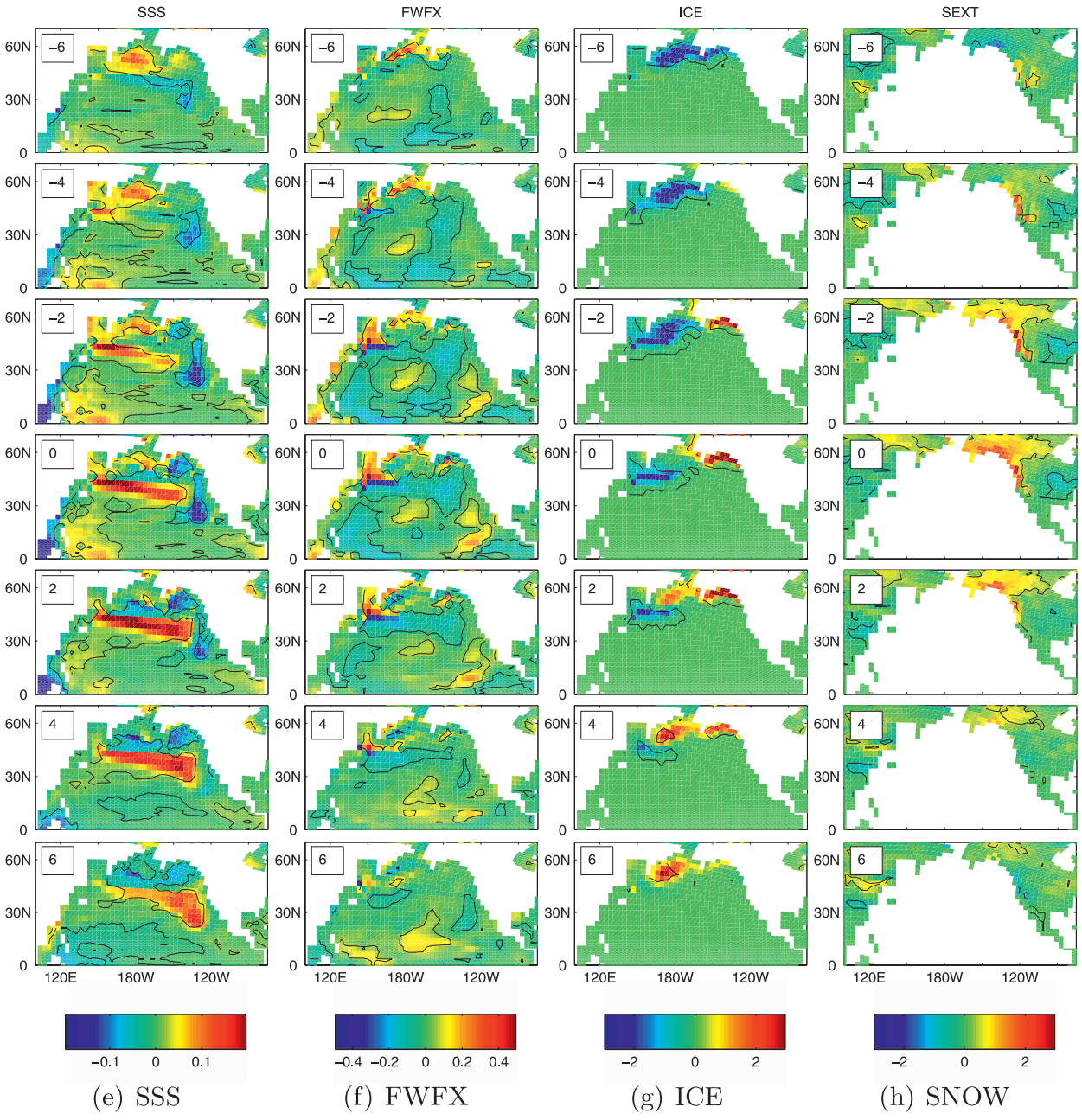

FIG. 9. (*Continued*)

to oceanic perturbations, the answer to this question must be sought in the variables that are in quadrature of phase with the mature phase of the PDO (i.e., with extrema at lags −6 and 6 yr).

At these lags of −6 and 6 yr, it is apparent that the heat flux anomaly in the Bering Sea reached its highest absolute value with opposite sign (Fig. 9d). In the Bering Sea, these extrema of the total heat flux anomaly correspond to extrema of both ocean–atmosphere and ocean–sea ice heat exchange anomalies (not shown); positive (negative) heat flux anomalies correspond to more (less) sea ice coverage and a cooling (warming) of the atmosphere. Sea ice anomalies in the North Pacific–Arctic region, by modulating the albedo and therefore the surface atmospheric temperature, are able to generate a wave train that extends downstream along the coast of North America (Honda et al. 1999; Alexander et al. 2004). It can be conjectured that the modulation of heat flux to the atmosphere from the Bering Sea would have the same effect [see, e.g., the study in the North

Atlantic by Deser et al. (2007)]. The opposite dipole structure of the wind stress curl anomaly at lags −6 and 6 yr is therefore likely to be explained by the concomitant sea ice and heat flux anomalies in the Bering Sea.[3]

6. Genesis of anomalies in the Bering Sea

Based on the detailed chronology of the simulated PDO presented in the previous section, the three key mechanisms for the development of the PDO appear to be (i) SST anomalies created by barotropic adjustment to Aleutian low pressure anomalies, (ii) a positive feedback between the SST anomalies created and the Aleutian low anomalies, and (iii) the development of anomalies in the Bering Sea in quadrature of phase with the PDO extrema that are able to trigger the reversal of PDO phase. The first two mechanisms are well represented in the existing literature concerning the PDO. To strengthen the plausibility of the last mechanism in the PDO development, which is original to this paper, this section attempts to explain the genesis of the Bering Sea anomaly and from it to justify the 20-yr time scale of the PDO.

In the development of the PDO, the positive anomaly in sea ice extent appears to propagate from the coast of Alaska into the Bering Sea (lags −2 to 6 yr; Fig. 9g). This westward propagation is in turn linked to the North American snow cover anomaly, which is characterized by a positive anomaly that propagates from the Rocky Mountains to Alaska (lags −4 to 4 yr; Fig. 9f). Such propagation is not expected to be an intrinsic feature of the snow and sea ice dynamics alone but rather the result of the change in the climatic conditions of the region.

The positive snow anomaly in the Rocky Mountains, which originates around lags −4 and −2 yr, is presumably due to the combination of the warmer SST in the western Pacific and the colder air above the Rocky Mountains (not shown). First, an excess of evaporation, resulting from the warmer SST, increases the moisture in the air (originating from the western Pacific Ocean) above North America. Then, the colder air above the Rocky Mountain (probably due to the weakening of the Aleutian low) favors the precipitation of this moisture.

The propagation of this positive snow cover anomaly from the Rocky Mountains to Alaska follows the extension to the north and the strengthening of the negative SST anomaly along the coast of North America from lags −4 to 0 yr (Fig. 9c). Subsequently, this negative SST anomaly seems to propagate westward together with the positive sea ice anomaly, reaching the Bering Sea around lag 4 yr. When it reaches the Bering Sea, these anomalously cold waters are therefore favorable for the onset of a positive sea ice anomaly.

Subsurface pathways

During its journey along the coast, this negative SST anomaly is generally associated with positive heat flux anomalies, which tend to diminish its amplitude. It may therefore be conjectured that, rather than solely involving the surface fluxes, the subsurface dynamics must play a role in maintaining the amplitude of the SST anomaly during the course of its journey.

Because this negative SST anomaly is coincident with a negative SSS anomaly (Figs. 9c,e), and because it follows the subpolar gyre circulation, this suggests that one must look for subsurface thermal anomalies, which are density compensated by salinity anomalies (i.e., ''spiciness'' anomalies; Munk 1981) and which may therefore be advected in the subsurface by the mean subpolar gyre.

To analyze and follow spiciness anomalies along their path of propagation, the salinity field is projected onto time-varying potential density surfaces. A spiciness anomaly is defined as the difference between the salinity on an isopycnal and the mean salinity on the same isopycnal. The same results presented hereafter would be found if temperature was used instead of salinity.

Away from boundary layers (mixed layers and horizontal boundaries) and assuming that mixing is weak in the interior ocean, then waters conserve both their density and Bernoulli function. Subject to this constraint, mean fluid trajectories may be approximated by the isopycnal projection of the Bernoulli function. The Bernoulli function is roughly approximated here by the depth of the isopycnals themselves.[4]

The time evolution of the spiciness anomaly on two isopycnals along the depth of 200 m is presented (in Fig. 10). The 200-m depth, together with two isopycnals, have been specifically chosen to represent the subsurface pathways from the deep winter mixed layer region in the center of action of the PDO to the most equatorial and most polar regions. Both pathways display clear

[3] We acknowledge that this dipole structure of the wind stress curl anomaly is weak and not statistically significant at the 90% level for lag 6 yr compared to lag −6 yr (Fig. 9a). However, this dipole is significant in the other simulation, 1990-control (not shown). Moreover its signature in terms of Sverdrup balance through the barotropic stream function anomaly is statistically significant at lag 6 yr (Fig. 9b). We suggest therefore that the weak amplitude of this dipole at lag 6 yr is due to only a global decorrelation time scale that is smaller between atmospheric and oceanic variables than between two oceanic variables.

[4] This corresponds to neglect of the velocity component of the Bernoulli function, an approximation that is acceptable in the interior ocean when comparing the variation of the depth of the isopycnals to the variation of velocity amplitude.

advection of spiciness anomalies from the Kuroshio Extension region to the equatorial and Bering Sea regions. For both pathways, the typical advection time scale is decadal, with a maximum of correlation coefficients attained for 10 yr between the star points and plus points in Fig. 10.

The two subsurface pathways, poleward and equatorward, could therefore be invoked to be responsible for setting up the 20-yr time scale of the PDO. However, from the development described in the previous section, it is clearly apparent that the tropical region is not strongly involved in the modeled PDO mechanism, in contrast with the Bering Sea. Two reasons can be invoked for discarding the equatorial pathway in favor of the poleward pathway. First, the initial spiciness anomaly amplitudes seem to decrease substantially before reaching the equator, probably because the equatorial pathway is much longer and/or because the mixing of subsurface waters is more vigorous in the tropics because of more intense currents. Second, the spiciness anomalies that reach the equator at 200-m depth are located beneath the strong tropical thermocline (Fig. 11), implying that important mixing will be involved before they can reach the surface, further diminishing their amplitude. In contrast, the poleward pathway is slow with weak currents and the density stratification in the Bering Sea is also weak, allowing spiciness anomalies at 200-m depth to reach the surface after experiencing less mixing than would be the case at the equator.

From both a surface and a subsurface point of view, the Bering Sea therefore appears to play a key role in the development of the PDO; the subsurface advection of spice anomalies formed in the central and western Pacific to the Bering Sea establishes the typical 10-yr time scale, and their reappearance at the surface in the Bering Sea is able to trigger the required reversal of the Aleutian low anomaly that initiates the second half cycle of the PDO.

7. Warming simulations

Having established what we believe to be the fundamental mechanism that underlies the PDO in the control simulations, we will investigate in this penultimate section of the paper the possible effect of global warming on the PDO by analyzing the five transient simulations described in section 2 whose properties were listed in Table 1.

The behavior of the natural variability of the North Pacific, (i.e., the PDO) in the presence of forcing, seems at first order to be independent of both the forcing amplitude and the initial quasi-steady state. In all the warming simulations we have performed, after having linearly detrended all time series, the classical PDO pattern always arises as the first EOF of SST with the same amplitude of 0.6° (i.e., Fig. 1 for the simulation 1870–2000). The value of variance that is explained by this first EOF is either equal to or larger than the value in the statistically equilibrated runs (from 43% in 1990–1.0% to 56% in 1990–0.5%). The fact that the spatial pattern of the warming trend, which shares the same structure[5] in all 5 simulations (i.e., Fig. 1 for the simulation 1870–2000), has a maximum located in the western and central region, just as the PDO itself, might indicate that the forced warming tends to interact with the dominant natural mode of variability, which is the PDO. This would explain why the modeled PDO explained slightly more variance in all the warming simulations than in the equilibrated runs.

Although the modeled PDO does not seem to be affected by the warming scenarios in terms of spatial features of SST, there is an evident and significant shift in terms of SSS variability, which occurs in three of the five warming simulations. In 1990–1.0%, 1870–1.0%, and 1990–0.5%, this SSS ''catastrophe'' occurs after approximately 90, 110, and 130 yr, respectively. After this event, much fresher surface conditions are found in the Bering and Okhotsk Seas (creating a strong halocline; Fig. 11) and the SSS variability comes to be dominated by a maximum of variance surrounding the Bering Strait (not shown).

A preliminary analysis of these three simulations shows that the change in SSS variability takes place simultaneously with the disappearance of the summer sea ice coverage in the Arctic Ocean. In 1990–1.0%, 1870–1.0%, and 1990–0.5%, by which time the sea ice extent has fallen to 40% in summer at approximately 90, 110, and 130 yr, respectively, there is a quick drop of the northward Bering Strait transport, which eventually stops or even reverses (Fig. 12). A discussion of the reason for the change of the mean SSS condition in the Bering Sea is beyond the scope of this paper, but it can be conjectured that, once the sea ice coverage disappears in the Arctic basin, the wind field comes to greatly influence the Arctic circulation, which leads to a change of the Bering Strait transport and to the subsequent freshening of the Bering Sea.

Prior to this event in 1990–1.0%, 1870–1.0%, and 1990–0.5% or in the complete simulations 1870–0.5% and 1870–2000, the first and second EOFs of SSS in the NP region have the same spatial structures as the first and second EOFs in the statistical equilibrium runs (Fig. 3). The time scale, which can be inferred from the time-lag

[5] The warming trend has a unique sign in the entire North Pacific for the four simulations with constant CO_2 increase.

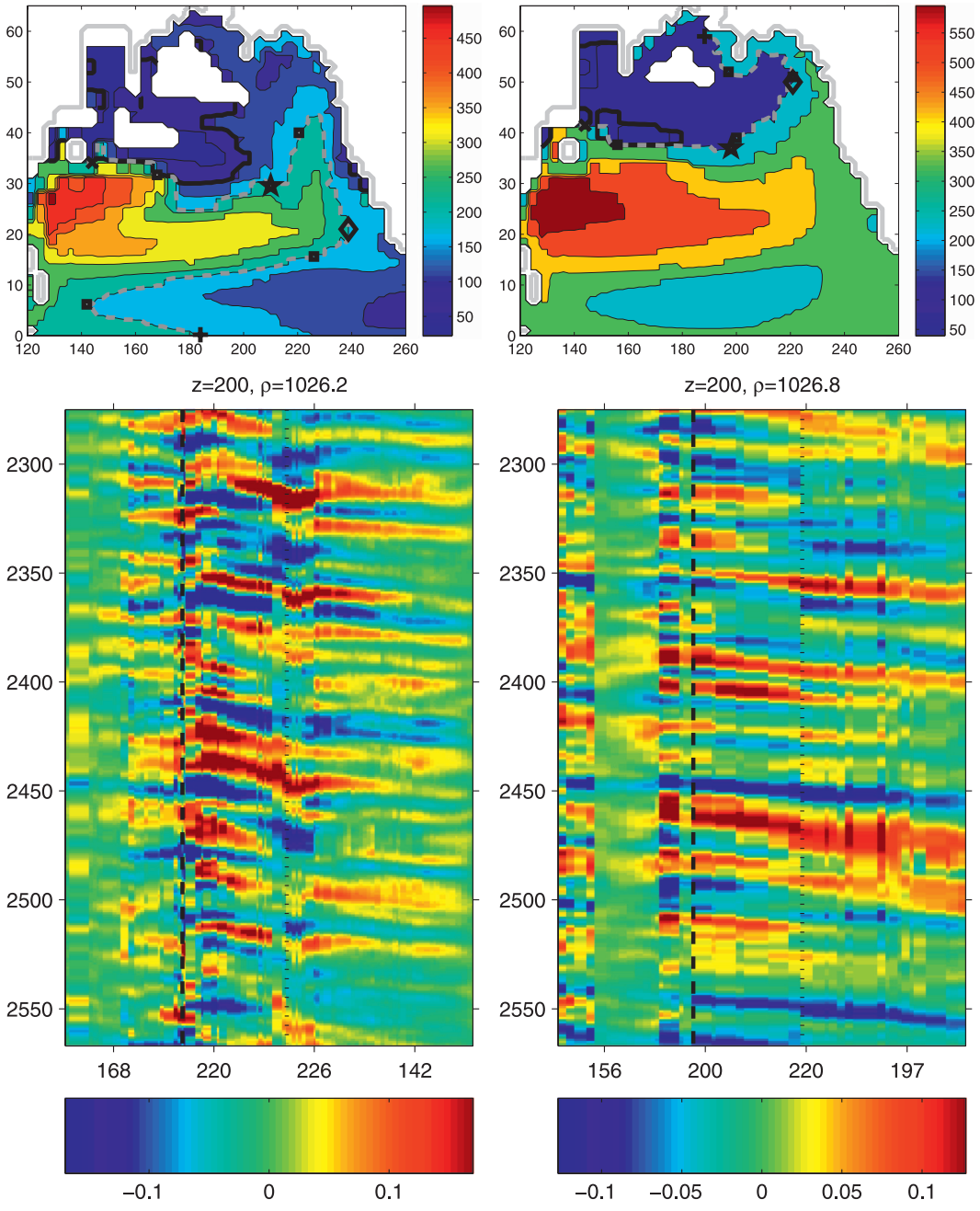

FIG. 10. Depth of the mean (top left) $\sigma_\theta = 26.2$ and (top right) $\sigma_\theta = 26.8$ isopycnals. The color bar is in meters, with isolines every 50 and 100 m, respectively. The light gray solid line delimits the continental coasts and white regions in the ocean domain correspond to areas where the isopycnal does not exist in the average. The thick solid line delimits where the mean winter mixed layer reached the plotted isopycnal. (bottom) Time–space diagram of spice anomaly (psu) along the 200-m isoline, highlighted in the panel above with a gray dashed line. (top) The abscissa axis following the 200-m isoline from the point noted with a crisscross to the point noted with a plus symbol is labeled with the longitude of the 200-m isoline points and its 4 tick marks correspond to the 4 points noted with solid squares. (bottom) The vertical dotted line corresponds to the most eastern point (open diamond). The vertical dashed line corresponds to the chosen point (star) for the time-lag correlation with the end of the isoline (plus symbol) discussed in the text.

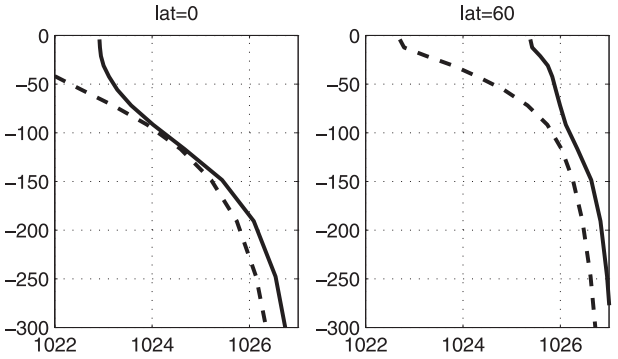

FIG. 11. Mean potential density (kg m^{-3}) profiles at (left) 0°N, 180°W and (right) 60°N, 180°W for 1870-control (solid line) and for the last 20 yr of 1870–1.0% (dashed line).

correlations of the principal components of these two EOFs, is on the same order of 20 yr as in the statistical equilibrium runs (Figs. 3, 13). This 20-yr time scale is also confirmed by spectral peaks in the PDO range for the first EOFs of SSS (not shown). This demonstrates that the same canonical PDO in all warming simulations is occurring prior to the SSS shift.

From the power spectrum analyses of the PDO SST indices (Fig. 14) the five warming simulations can be separated into two categories depending on the strength of the forcing. For the simulations with the largest forcing (1870–1.0% and 1990–1.0%), no significant decadal peaks are found in the spectra that are entirely dominated by lower frequencies. For the simulations with weak or moderate warmings (1870–2000, 1870–0.5%, and 1990–0.5%), the spectra are dominated by a decadal peak significant at the 95% level in the PDO frequency range; however, for these three simulations, the spectra also display some power at lower frequencies. This power at multidecadal periods is statistically significant at the 90% level in 1870–0.5% and 1990–0.5% (the simulation 1870–2000 is suspected to be too short to have significant power at multidecadal periods).

In conclusion, the detrended variability signal in the North Pacific, in the presence of a forced warming, displays significant power at multidecadal frequencies in all simulations. The persistence of the canonical PDO (i.e., the natural North Pacific variability as characterized in the control simulations) as the leading mode of variability depends on the strength of the forcing. If the warming is too strong, then the typical time scale of 20 yr of the canonical PDO can no longer be detected, except in terms of SSS variability and only prior to a change of the Bering Strait Throughflow.

8. Discussion

a. On the mechanism of the PDO

The modeled Pacific Decadal Oscillation (PDO) has been confirmed in this study to result primarily from a basin-wide ocean adjustment to changes of the atmospheric forcing associated with the Aleutian low pressure region (Latif and Barnett 1996; Pierce et al. 2001; Schneider et al. 2002; Latif 2006; Kwon and Deser 2007). We find that three elements are required to create the PDO cycle in the CCSM3 model that we have employed. First, initial SST anomalies are created by the fast

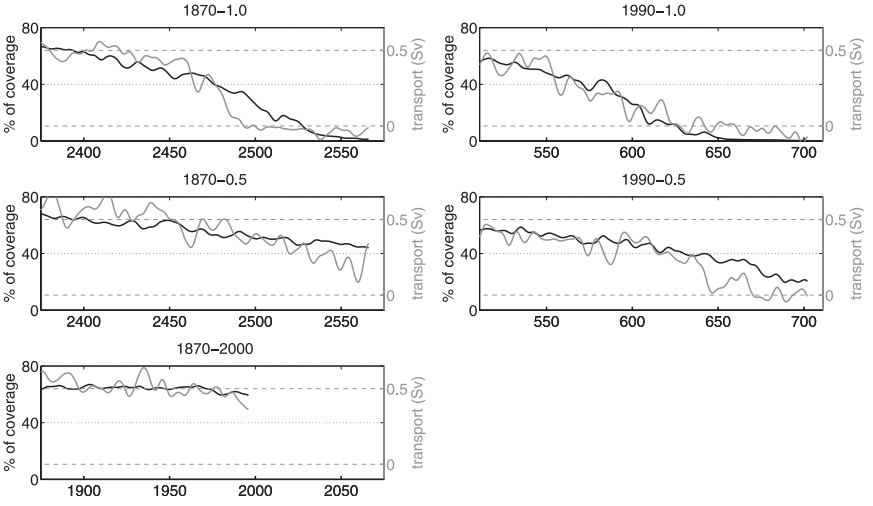

FIG. 12. Sea ice coverage in the Arctic Ocean (north of 65°N) (%; black line, left axis) and Bering Strait transport in Sv (gray line, right axis) in the five warming simulations: (top left) 1870–1.0%, (top right) 1990–1.0%, (middle left) 1870–0.5%, (middle right) 1990–0.5%, and (bottom left) 1870–2000. The indices have been low-pass filtered.

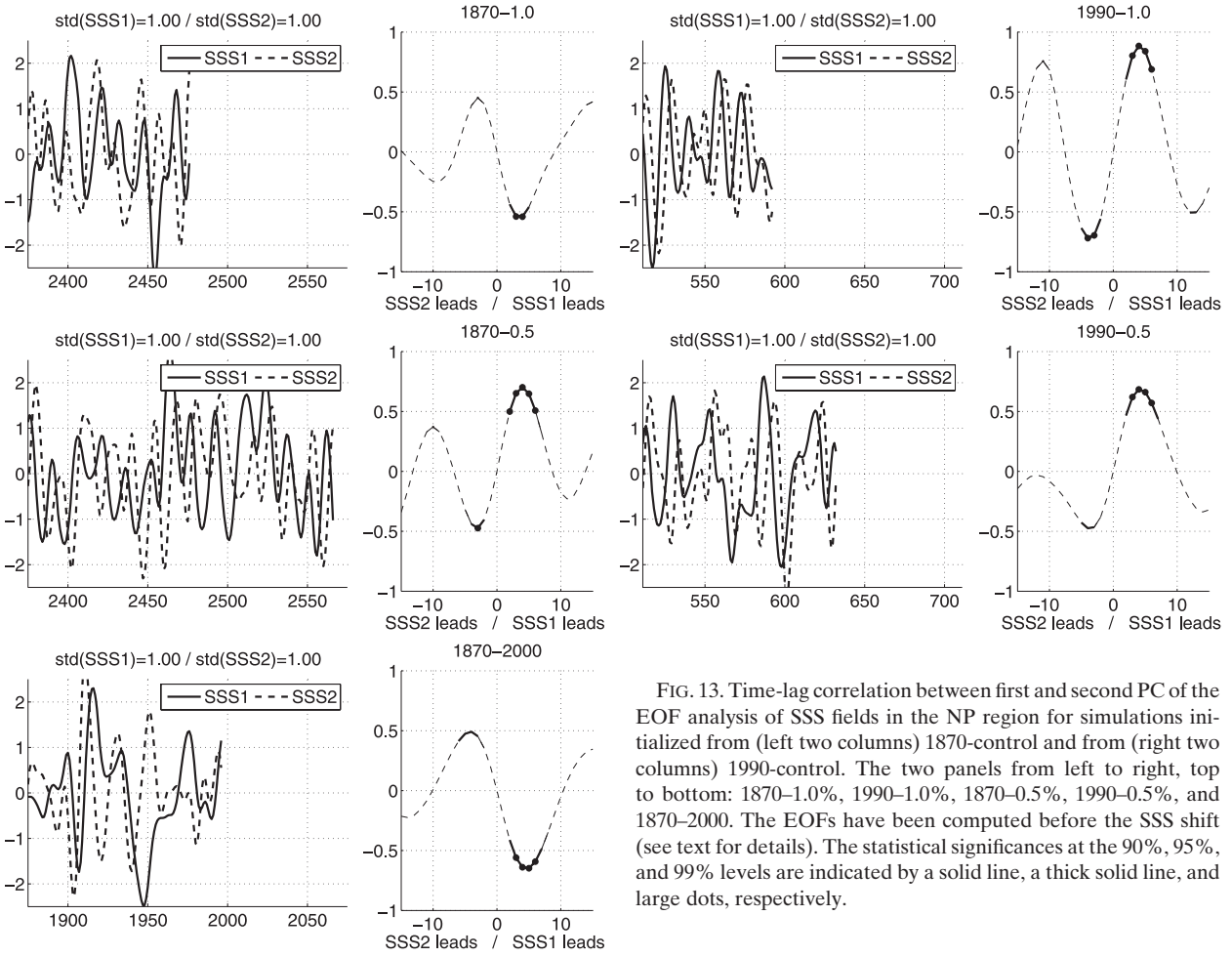

FIG. 13. Time-lag correlation between first and second PC of the EOF analysis of SSS fields in the NP region for simulations initialized from (left two columns) 1870-control and from (right two columns) 1990-control. The two panels from left to right, top to bottom: 1870–1.0%, 1990–1.0%, 1870–0.5%, 1990–0.5%, and 1870–2000. The EOFs have been computed before the SSS shift (see text for details). The statistical significances at the 90%, 95%, and 99% levels are indicated by a solid line, a thick solid line, and large dots, respectively.

barotropic adjustment to the initial Aleutian low anomalies. Second, a positive feedback between the SST and the Aleutian low anomalies is responsible for the growth phase of the PDO. Finally, the appearance of temperature anomalies in the Bering Sea in phase quadrature with the PDO extrema anomalies is able to trigger the reversal of PDO phase.

According to this novel hypothesis, salinity plays a key role in permitting the existence of density-compensated thermal anomalies, which are advected in the subsurface by the subpolar gyre. The advection from the western and central North Pacific to the Bering Sea has a typical time scale of 10 yr and is therefore a very likely rationale for the 20-yr time scale of the modeled PDO in the control simulations.

This mechanism is in contrast to the generally accepted idea that the PDO time scale is set by the westward propagation of baroclinic Rossby waves triggered by the geostrophic adjustment to Aleutian low variability. Our analysis does acknowledge the possible importance of baroclinic adjustment in the development of one half a cycle of the PDO. However, we have not been able to identify any evidence of baroclinic westward propagation with decadal time scale in the latitudinal band that passes through the center of action of the PDO. As acknowledged in many previous analyses since the seminal studies of Latif and Barnett (1994, 1996), advection dominates in the Kuroshio Extension. Another pathway must therefore be found to propagate any sort of information. More analyses will clearly be needed to confirm or deny the ''Rossby wave hypothesis,'' but the mechanism suggested here is a highly plausible alternative.

The modeled PDO in CCSM3 differs from the observed PDO by the absence of a surface linkage to the tropics. This emphasizes first that significant forcing from the tropics is not required for a mode with PDO-like variability to exist (Latif 2006; Kwon and Deser 2007; Zhong et al. 2007). However, it does not rule out the possibility of an important role being played by the tropics in the observed PDO. The influence of ENSO on

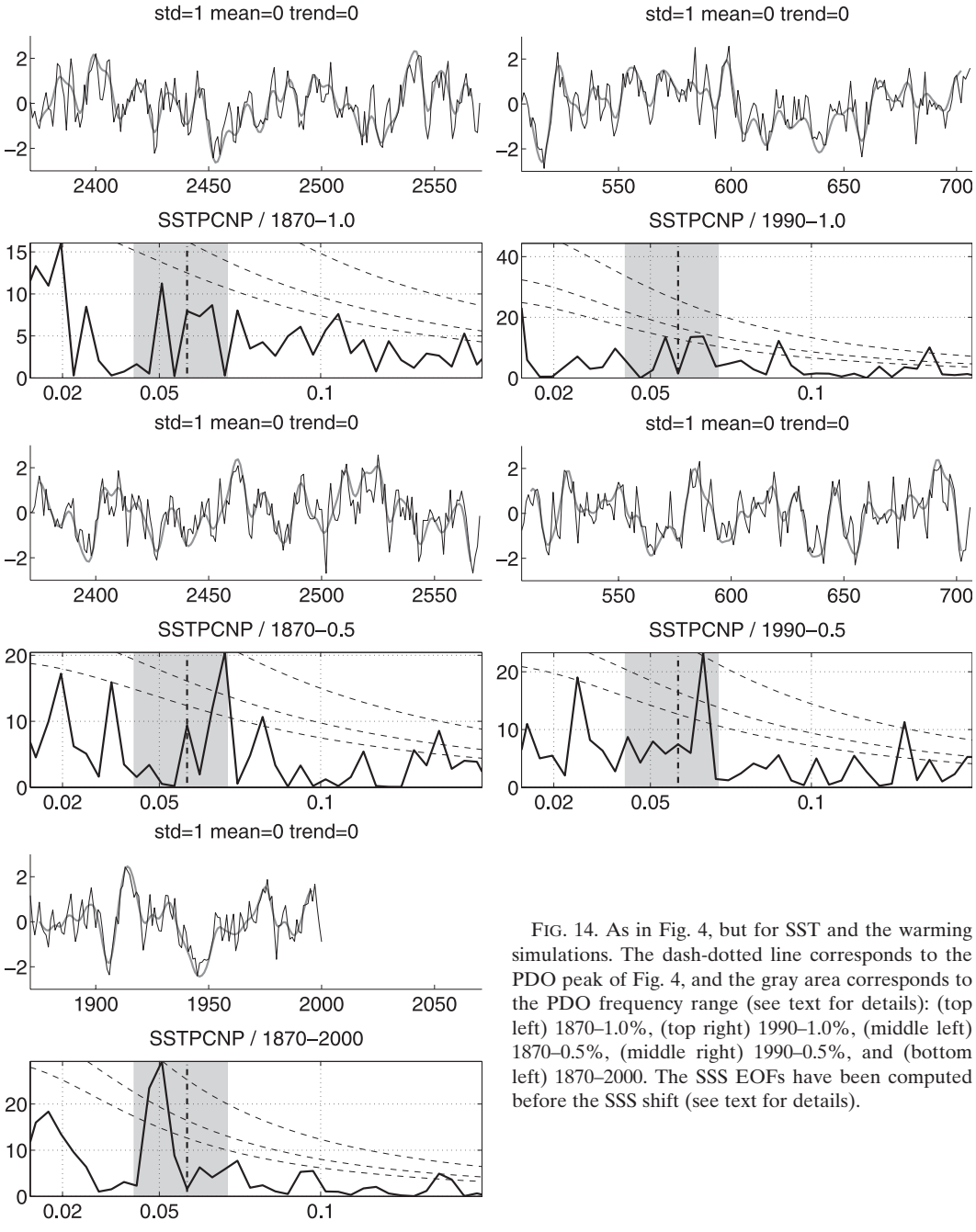

FIG. 14. As in Fig. 4, but for SST and the warming simulations. The dash-dotted line corresponds to the PDO peak of Fig. 4, and the gray area corresponds to the PDO frequency range (see text for details): (top left) 1870–1.0%, (top right) 1990–1.0%, (middle left) 1870–0.5%, (middle right) 1990–0.5%, and (bottom left) 1870–2000. The SSS EOFs have been computed before the SSS shift (see text for details).

midlatitude Pacific SSTs has been the focus of many studies that argue for a direct forcing of ENSO on the PDO (Alexander et al. 2002; Newman et al. 2003). A further source of ENSO influence on midlatitudes is through its ability to modify the Aleutian low, which further reinforces it as a candidate trigger mechanism for the PDO phase reversal (Masuda 2002). Although density-compensated thermal anomalies are able to reach the equator in CCSM3 as demonstrated here (see also Schneider 2000), the classical "oceanic tunnel" (Gu and Philander 1997) does not allow the modulation of ENSO by the PDO in CCSM3, probably because of excessive mixing of the thermal anomalies on their way to the tropics and also the existence of the shallow equatorial thermocline. This may be why the reversing mechanism is not seen to arise from ENSO in our simulations, even if the typical advection time scale to the tropics would also be on the order of 10 yr.

Sea ice anomalies create robust seasonal responses of the atmosphere, both locally and globally. However, the global responses for the SST or the snow coverage anomalies usually have a small amplitude compared to the atmospheric noise, which requires large ensembles of numerical simulations to assess their statistical significance (Alexander et al. 2004; Deser et al. 2007; Fletcher et al. 2007). One might imagine that a seasonal sea ice anomaly should be sufficient for the prediction of a local atmospheric anomaly. In the context of decadal variability, if a sea ice anomaly persists for a few years, then the atmosphere is more likely to develop a robust global response. The persistence of oceanic SST and SSS anomalies is therefore key to the maintenance of a sea ice anomaly that is able to switch the sign of the Aleutian low anomaly in order to change the phase of the modeled PDO.

b. On the effect of global warming

The SSS variability that characterizes the PDO and its time scale of 20 yr in the control simulations has been demonstrated to be initially unchanged under forced warming. This means that the mechanism responsible for the natural PDO (i.e., described in the control simulations) is still working even in the presence of this secular influence.

However, it has been shown that under the influence of global warming the PDO SST index displays significant power at multidecadal time scales, which can even dominate the 20-yr time-scale variability of the natural PDO when warming is intense (i.e., 1% increase of CO_2 concentration per year). Because the spatial pattern of dominant SST variability under forced warming does not differ substantially from the classical horseshoe pattern of the PDO, this indicates that the forced warming either modulates the natural PDO with lower frequency or excites another low-frequency mechanism, which reinforces the PDO in the sense that it has the same surface signature.

This effect of a forced warming on the PDO, seen in the present study, could help to explain why a change of the PDO time scale (from 20 yr to a longer period in the last century) has been suggested on the basis of a tree ring chronology for the last 300 yr (Biondi et al. 2001). This would also be in agreement with the fact that the PDO index based on SST reconstructions for the last 130 yr, during which global warming is acting, displays two different time scales at 20 and 60 yr (d'Orgeville and Peltier 2007).

In the warming experiments, an important event is the moment when the summer Arctic sea ice totally disappears, after approximately 90–200 yr in our simulations, depending on both the strength of the warming and the initial state (this ''tipping point'' prediction could be strongly dependent on model resolution). In the North Pacific, this change of the Arctic circulation leads to the arrest of the northward Bering Strait transport, a subsequent change of the Bering Sea hydrology (with much fresher surface water), and therefore a direct influence on the decadal variability in the entire basin. As described in the second part of this study (d'Orgeville and Peltier 2009), a large freshening of the Labrador Sea also occurs around the same time and simultaneously impacts the multidecadal variability of the North Atlantic. Those two results highlight the fact that the disappearance of summer sea ice in the Arctic will not only impact precipitation and weather patterns (Serreze et al. 2007) but also modes of variability with much longer time scales.

Acknowledgments. The work reported in this paper is a contribution to the Polar Climate Stability Network, which is funded by the Canadian Foundation for Climate and Atmospheric Science. Additional support was provided by NSERC Grant 9627.

REFERENCES

Alexander, M. A., I. Blade, M. Newman, J. R. Lanzante, N.-C. Lau, and J. D. Scott, 2002: The atmospheric bridge: The influence of ENSO teleconnections on air–sea interaction over the global oceans. *J. Climate,* **15,** 2205–2231.

——, U. S. Bhatt, J. E. Walsh, M. S. Timlin, J. S. Miller, and J. D. Scott, 2004: The atmospheric response to realistic Arctic sea ice anomalies in an AGCM during winter. *J. Climate,* **17,** 890–905.

——, and Coauthors, 2006: Extratropical atmosphere–ocean variability in CCSM3. *J. Climate,* **19,** 2496–2525.

Biondi, F., A. Gershunov, and D. R. Cayan, 2001: North Pacific decadal variability since 1661. *J. Climate,* **14,** 5–10.

Boccaletti, G., R. C. Pacanowski, and S. G. H. Philander, 2005: A diabatic mechanism for decadal variability in the tropics. *Dyn. Atmos. Oceans,* **39,** 3–19.

Bretherton, C. S., M. Widmann, V. P. Dymnikov, J. M. Wallace, and I. Bladé, 1999: The effective number of spatial degrees of freedom of a time-varying field. *J. Climate,* **12,** 1990–2009.

Collins, W. D., and Coauthors, 2006: The Community Climate System Model version 3 (CCSM3). *J. Climate,* **19,** 2122–2143.

Deser, C., A. S. Phillips, and J. W. Hurrel, 2004: Pacific interdecadal climate variability: Linkages between the tropics and the North Pacific during boreal winter since 1900. *J. Climate,* **17,** 3109–3124.

——, R. A. Tomas, and S. Peng, 2007: The transient atmospheric circulation response to North Atlantic SST and sea ice anomalies. *J. Climate,* **20,** 4751–4767.

Di Lorenzo, E., and Coauthors, 2008: North Pacific gyre oscillation links ocean climate and ecosystem change. *Geophys. Res. Lett.,* **35,** L08607, doi:10.1029/2007GL032838.

d'Orgeville, M., and W. R. Peltier, 2007: On the Pacific Decadal Oscillation and the Atlantic Multidecadal Oscillation: Might they be related? *Geophys. Res. Lett.,* **34,** L23705, doi:10.1029/2007GL031584.

——, and ——, 2009: Implications of both statistical equilibrium and global warming simulations with CCSM3. Part II: On the multidecadal variability in the North Atlantic basin. *J. Climate,* **22,** 5298–5318.

Fletcher, C. G., P. J. Kushner, and J. Cohen, 2007: Stratospheric control of the extratropical circulation response to surface forcing. *Geophys. Res. Lett.,* **34,** L21802, doi:10.1029/2007GL031626.

Gershunov, A., and T. P. Barnett, 1998: Interdecadal modulation of ENSO teleconnections. *Bull. Amer. Meteor. Soc.,* **79,** 2715–2725.

Gu, D., and S. G. H. Philander, 1997: Interdecadal climate fluctuations that depend on exchanges between the tropics and extratropics. *Science,* **275,** 805–807.

Honda, M., K. Yamazaki, H. Nakamura, and K. Takeuchi, 1999: Dynamic and thermodynamic characteristics of the atmospheric response to anomalous sea-ice extent in the Sea of Okhotsk. *J. Climate,* **12,** 3347–3358.

Kwon, Y.-O., and C. Deser, 2007: North Pacific decadal variability in the Community Climate System Model version 2. *J. Climate,* **20,** 2416–2433.

Latif, M., 2006: On North Pacific multidecadal climate variability. *J. Climate,* **19,** 2906–2915.

——, and T. P. Barnett, 1994: Causes of decadal climate variability over the North Pacific and North America. *Science,* **266,** 634–637.

——, and ——, 1996: Decadal variability over the North Pacific and North America: Dynamics and predictability. *J. Climate,* **9,** 2407–2423.

Mann, M., and J. Lees, 1996: Robust estimation of background noise and signal detection in climatic time series. *Climatic Change,* **33,** 409–445.

Mantua, N. J., S. R. Hare, Y. Zhang, J. M. Wallace, and R. C. Francis, 1997: A Pacific interdecadal climate oscillation with impacts on salmon production. *Bull. Amer. Meteor. Soc.,* **78,** 1069–1079.

Masuda, S., 2002: Role of the ocean in the decadal climate change in the North Pacific. *J. Geophys. Res.,* **107,** 3224, doi:10.1029/2002JC001420.

McCabe, G. J., and M. D. Dettinger, 1999: Decadal variations in the strength of ENSO teleconnections with precipitation in the western United States. *Int. J. Climatol.,* **19,** 1399–1410.

Meehl, G. A., and Coauthors, 2006: Climate change projections for the twenty-first century and climate change commitment in the CCSM3. *J. Climate,* **19,** 2597–2616.

Minobe, S., 1997: A 50–70 year climatic oscillation over the North Pacific and North America. *Geophys. Res. Lett.,* **24,** 683–686.

Munk, W., 1981: Internal waves and small-scale processes. *Evolution of Physical Oceanography,* B. A. Warren and C. Wunsch, Eds., M.I.T. Press, 264–291.

Neelin, J. D., and W. Weng, 1999: Analytical prototypes for ocean–atmosphere interaction at midlatitudes. Part I: Coupled feedbacks as a sea surface temperature dependent stochastic process. *J. Climate,* **12,** 697–721.

Newman, M., G. P. Combo, and M. A. Alexander, 2003: ENSO-forced variability of the Pacific decadal oscillation. *J. Climate,* **16,** 3853–3857.

Peltier, W. R., and L. P. Solheim, 2004: The climate of the earth at Last Glacial Maximum: statistical equilibrium state and a mode of internal variability. *Quat. Sci. Rev.,* **23,** 335–357.

Pierce, D. W., T. P. Barnett, N. Schneider, R. Saravanan, D. Dommenget, and M. Latif, 2001: The role of ocean dynamics in producing decadal climate variability in the North Pacific. *Climate Dyn.,* **18,** 51–70.

Saravanan, R., and J. C. McWilliams, 1997: Stochasticity and spatial resonance in interdecadal climate fluctuations. *J. Climate,* **10,** 2299–2320.

——, and ——, 1998: Advective ocean–atmopshere interaction: An analytical stochastic model with implication for decadal variability. *J. Climate,* **11,** 165–188.

Schneider, N., 2000: A decadal spiciness mode in the tropics. *Geophys. Res. Lett.,* **27,** 257–260.

——, A. J. Miller, and D. W. Pierce, 2002: Anatomy of North Pacific decadal variability. *J. Climate,* **15,** 586–605.

Seager, R., Y. Kushnir, N. H. Naik, M. A. Cane, and J. Miller, 2001: Wind-driven shifts in the latitude of the Kuroshio Oyashio Extension and generation of SST anomalies on decadal timescales. *J. Climate,* **14,** 4249–4265.

Serreze, M. C., M. M. Holland, and J. Stroeve, 2007: Perspectives on the Arctic's shrinking sea-ice cover. *Science,* **315,** 1533–1536.

Trenberth, K. E., 1990: Recent observed interdecadal climate changes in the Northern Hemisphere. *Bull. Amer. Meteor. Soc.,* **71,** 988–993.

——, and J. W. Hurrell, 1994: Decadal atmosphere-ocean variations in the Pacific. *Climate Dyn.,* **9,** 303–319.

Vimont, D. J., D. S. Battisti, and A. C. Hirst, 2001: Footprinting: A seasonal connection between the tropics and mid-latitudes. *Geophys. Res. Lett.,* **28,** 3923–3926.

Wu, X., L. Deng, X. Song, G. Vettoretti, W. R. Peltier, and G. J. Zhang, 2007: Impact of a modified convective scheme on the Madden-Julian Oscillation and El Niño–Southern Oscillation in a coupled climate model. *Geophys. Res. Lett.,* **34,** L16823, doi:10.1029/2007GL030637.

Yeager, S. G., C. A. Shields, W. G. Large, and J. J. Hack, 2006: The low-resolution CCSM3. *J. Climate,* **19,** 2545–2566.

Zhang, Y., J. M. Wallace, and D. S. Battisti, 1997: ENSO-like interdecadal variability: 1900–93. *J. Climate,* **10,** 1004–1020.

Zhong, Y., Z. Liu, and R. Jacob, 2007: Origin of Pacific multidecadal variability in Community Climate System Model version 3 (CCSM3): A combined statistical and dynamical assessment. *J. Climate,* **21,** 114–133.